METALLURGY

In situ design of advanced titanium alloy with concentration modulations by additive manufacturing

Tianlong Zhang[1,2], Zhenghua Huang[3], Tao Yang[1]*, Haojie Kong[1], Junhua Luan[1], Anding Wang[1], Dong Wang[2], Way Kuo[1], Yunzhi Wang[4]*, Chain-Tsuan Liu[1]*

Additive manufacturing is a revolutionary technology that offers a different pathway for material processing and design. However, innovations in either new materials or new processing technologies can seldom be successful without a synergistic combination. We demonstrate an in situ design approach to make alloys spatially modulated in concentration by using laser-powder bed fusion. We show that the partial homogenization of two dissimilar alloy melts—Ti-6Al-4V and a small amount of 316L stainless steel—allows us to produce micrometer-scale concentration modulations of the elements that are contained in 316L in the Ti-6Al-4V matrix. The corresponding phase stability modulation creates a fine scale–modulated β + α′ dual-phase microstructure that exhibits a progressive transformation-induced plasticity effect, which leads to a high tensile strength of ~1.3 gigapascals with a uniform elongation of ~9% and an excellent work-hardening capacity of >300 megapascals. This approach creates a pathway for concentration-modulated heterogeneous alloy design for structural and functional applications.

Additive manufacturing (AM), also referred to as three-dimensional (3D) printing, integrates multiple metallurgical processes into one in which the making, shaping, and treating of alloys take place all at once in a single process (*1*–*8*). However, AM has largely been regarded as a forming technology that produces material components near net shape, without taking full advantage of the capabilities offered by AM for simultaneous and synergistic advancements of both alloy and process together (*2*, *9*–*12*). By building a component flexibly point by point and layer by layer, AM provides the opportunity to create heterogeneous alloys with location-specific compositions and microstructures (*8*, *13*–*15*). During the laser-powder bed fusion (L-PBF), because of the short lifetime and fast cooling of the melt pool, even finer-scale (such as micrometer-scale) concentration modulations (microCMs hereafter) can be achieved through partial homogenization within each melt pool by using a premixed mixture of different alloy or elemental powders (*13*, *14*). Such microCMs have been shown to have the potential to offer various alloy-specific benefits, such as a gradient precipitate microstructure in β-Ti (*16*); martensite-austenite heterostructures in steels (*17*, *18*); and controlled strain release, linear superelasticity, and ultralow elastic modulus in ferroelastic materials (*19*, *20*).

We have demonstrated how to design such a microCM Ti alloy through L-PBF by using a mixture of two commercial alloy powders: Ti-6Al-4V (Ti64) and 316L (67.5Fe-18Cr-12Ni-2.5Mo, both in wt %). The choice of these two alloys is based on the following considerations. Ti64 by means of AM has long suffered from the problem of both large detrimental columnar grains and poor work-hardening capacity (*21*–*24*). The elements in 316L (Fe, Cr, Ni, and Mo; we refer to these as 316L elements) are effective grain refiners (*25*, *26*) and also effective β stabilizers in Ti alloys. In addition, high-quality powders of both alloys are commercially available for L-PBF (*27*). With an appropriate choice of the amount of 316L to be added and the L-PBF processing parameters, microCMs of these elements in the Ti64 matrix are created, and the corresponding phase stability modulation that is associated with the concentration modulation results in a fine-scale modulated β + α′ dual-phase microstructure in the as-printed alloy. This type of microCM Ti alloy exhibits a high yield strength and a progressive transformation-induced plasticity (TRIP) effect in a broad range of external loads during deformation (*19*, *20*, *28*), which leads to a prolonged uniform elongation and enhanced work-hardening effect.

The typical microCM architecture in the as-printed Ti64-(4.5%)316L (wt %) alloy is shown in Fig. 1, A to C. For example, our scanning electron microscopy–energy-dispersive spectroscopy (SEM-EDS) images (Fig. 1A) show obvious depletion of Ti, Al, and V (Ti64 elements) and enrichment of Fe, Cr, and Ni (316L elements) in one of the swirls within the melt pool. Higher-magnification transmission electron microscopy–EDS (TEM-EDS) line scan results (Fig. 1, B and C) illustrate clearer intragranular concentration gradients alongside the α′-β interphase interface region. The α′ martensitic phase regions have a much lower content of the 316L elements (the β stabilizers) as compared with that of the β phase regions. At the center of one of the α′ and one of the β phase regions, the precise compositions we measured with 3D atom probe tomography (3D-APT) (table S1) are Ti-6.0Al-4.1V-0.9Fe-0.3Cr-0.1Ni-0.01Mo and Ti-5.8Al-3.9V-6.4Fe-1.7Cr-1.6Ni-0.3Mo, respectively [which can also be simplified as Ti64-(1.3%)316L and Ti64-(9.9%)316L]. Therefore, the microCM alloy has location-specific compositions throughout the build.

The microCM is produced through partial homogenization of the two alloy melt swirls in the melt pool during L-PBF (*13*, *14*), in which both physical mixing by means of fluid flow with Marangoni motion and chemical mixing by means of atomic diffusion occur between the two alloy melts within the melt pool (*29*, *30*). Although the physical mixing tends to homogenize the melt at the melt-pool scale (creating swirls of the two alloy melts), a complete homogenization (for example, complete dissolution of the 316L elements into Ti64) requires sufficient chemical mixing—sufficient interdiffusion between the adjacent 316L element–rich and Ti64 element–rich swirls in the melt pool. Because of the small melt-pool size and rapid solidification associated with L-PBF (*31*, *32*), a partially homogenized state is preserved after solidification. The measured 316L concentration variation in the microCM Ti64-(4.5%)316L alloy by means of APT, TEM-EDS, and SEM-EDS ranges from ~1.3 to ~9.9 wt % ($\Delta c \approx$ 8.6 wt %) (table S1). This sort of concentration nonuniformity has been both reported and considered undesirable for AM (*13*, *14*, *33*, *34*). However, we actively used this characteristic of L-PBF to achieve microCMs in Ti alloys that lead to a modulated dual-phase (α′ + metastable β) microstructure with excellent mechanical properties.

One direct impact of the microCM is on the phase stability and microstructure modulation in the as-printed alloy. From a side-view cross section of the as-printed Ti64-(4.5%)316L, by using backscattered electron (BSE) imaging, we observed a lava-like microstructure that showed clear swirl patterns of the fluid flow within the melt pools (Fig. 1, D and E). Within each individual melt-pool region, we found two distinct microstructural features within the dark (316L element–poor) and bright (316L element–rich) swirls. The dark swirls consist of fine acicular α′ martensite (yellow arrows) with a typical lath thickness of ~100 nm, along with some ultrafine twin structures (~20 nm of twin spacing) inside (Fig. 1, F and G). The bright swirls, however, consist of a single β phase with a cellular microstructure at the center (blue arrows). We

[1]Department of Materials Science and Engineering, Hong Kong Institute for Advanced Study, College of Science and Engineering, City University of Hong Kong, Hong Kong, China. [2]Center of Microstructure Science, Frontier Institute of Science and Technology, State Key Laboratory for Mechanical Behavior of Materials, Xi'an Jiaotong University, Xi'an 710049, China. [3]Guangdong–Hong Kong Joint Research and Development Center on Advanced Manufacturing Technology for Light Alloys, Institute of New Materials, Guangdong Academy of Sciences, Guangzhou 510650, China. [4]Department of Materials Science and Engineering, Ohio State University, Columbus, OH 43210, USA.
*Corresponding author. Email: taoyang6-c@my.cityu.edu.hk (T.Y.); wang.363@osu.edu (Y.W.); chainliu@cityu.edu.hk (C.-T.L.)

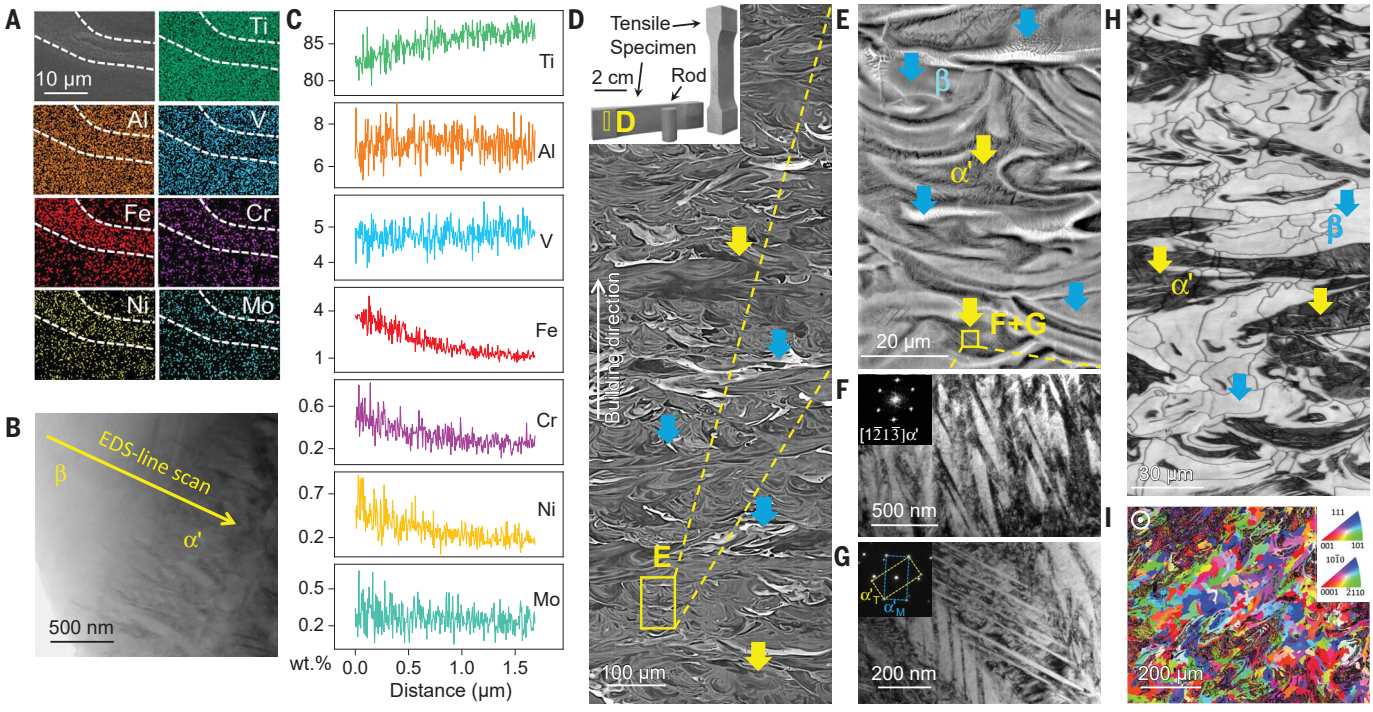

Fig. 1. Micrometer-scale concentration modulation and microstructures of the as-printed Ti64-(4.5%)316L alloy. (**A**) SEM-EDS maps showing the micrometer-scale depletion of Ti, Al, and V and enrichment of Fe, Cr, and Ni elements within one of the swirls of the melt pool. (**B**) Scanning TEM image of the β-α′ interphase region. The yellow arrow denotes the EDS line scan direction in (C). (**C**) Composition profiles across the β-α′ interphase boundary in (B) showing the enrichment of 316L elements (Fe, Cr, Ni, and Mo) in the β phase and depletion of 316L elements in the α′ phase. (**D**) Side-view cross-sectional BSE image showing lava-like microstructure with the clear swirl pattern from Marangoni convection during mechanical mixing in the melt pool. Brighter regions are enriched in heavy elements (Fe, Cr, Ni, and Mo in 316L, blue arrows), and darker regions are enriched in light elements (Ti, Al, and V in Ti64, yellow arrows). The inset shows a photograph of the as-printed Ti64-(4.5%)316L tensile specimen and rod. (**E**) Enlarged BSE image showing the lava-like heterogeneous microstructure with the coexistence of acicular α′ martensite (yellow arrows) and ultrafine β grains with solidification cellular structure (blue arrows). (**F**) Fine acicular α′ martensite as observed by TEM bright-field image. (**G**) Ultrafine twin structure as observed by TEM bright-field image. (**H** and **I**) EBSD images of as-printed Ti64-(4.5%)316L. (H) Band contrast image of side-view cross section showing the ultrafine grain structure without columnar grains. The bright regions (blue arrows) consist of bulk β grains, and the dark regions (yellow arrows) consist of fine acicular α′ martensite. (I) Inverse pole figure (IPF) map of the top-view cross section showing grain orientations of β and α′ phases.

confirmed the highly heterogeneous and fine-scale modulated β + α′ microstructure by using electron backscatter diffraction (EBSD) results (Fig. 1, H and I). Instead of the conventional large columnar grains along the build direction observed in AM Ti64 (*35*–*37*), there are ultrafine grains throughout the build. In addition, the as-printed alloy has a high density (>99.9%) (fig. S1).

The second impact of the microCM is on the metastability-induced mechanical property enhancement. Upon solidification, there exist 316L element–rich and 316L element–poor regions that are due to partial homogenization. Upon further cooling, the 316L element–poor regions undergo the β-to-α′ martensitic transformation, and the 316L element–rich regions are retained as metastable β phase, which creates a highly dispersed β + α′ dual-phase microstructure. Furthermore, the composition variation within the β phase regions leads to a phase stability variation (*28*), which results in a progressive TRIP effect upon loading and, thus, an excellent work-hardening capacity and prolonged uniform elongation. We performed tensile tests on the as-printed Ti64-(4.5%)316L microCM alloy (Fig. 2A) and obtained a yield strength (σ_γ) of 984 ± 14 MPa, an ultimate tensile strength (σ_{UTS}) of 1297 ± 10 MPa, and a uniform elongation (ε_u) of 8.8 ± 0.2% (Fig. 2A) with a ductile fracture mode (fig. S6). Compared with all classes of Ti alloys (α, α + β, and β) that are manufactured by different AM technologies (such as L-PBF, electron beam–PBF (E-PBF), and laser-directed energy deposition (L-DED)] (Fig. 2B and fig. S7) (*22*, *38*–*47*), the microCM Ti64-(4.5%)316L alloy exhibits simultaneously a higher σ_{UTS} and larger ε_u, which breaks the tradeoff between strength and ductility. In addition, the excellent work-hardening ability ($\sigma_{UTS} - \sigma_y$ = 313 ± 11 MPa) is advantageous in structural applications to guarantee a large safety margin before fracture (*48*).

Most additively manufactured Ti alloys lack substantial work hardening (*1*, *47*, *49*). Advanced AM-fabricated Ti64 can achieve a UTS of ~1.2 GPa (*43*, *49*). However, an early onset of plastic instability is usually observed, which leads to a premature failure before ε reaches 4% (Fig. 2B) (*43*, *49*). In general, the β phase volume fraction in as-printed or heat-treated Ti64 ranges from ~0 to 7% (*43*, *49*), whereas in our microCM Ti64-(4.5%)316L alloy, the β phase volume fraction reaches as high as 60% (Fig. 2C). This high-volume fraction is not surprising because all the four elements (Fe, Cr, Ni, and Mo) in 316L powders are strong β stabilizers in Ti alloys. Thus, in the microCM Ti64-(4.5%)316L alloy, the regions enriched in these elements remain as β even under the extremely high cooling rates during L-PBF. However, alloys with a large volume fraction of β phase may not necessarily have an enhanced work-hardening ability. For example, the microCM Ti64-(6.0%)316L alloy consists

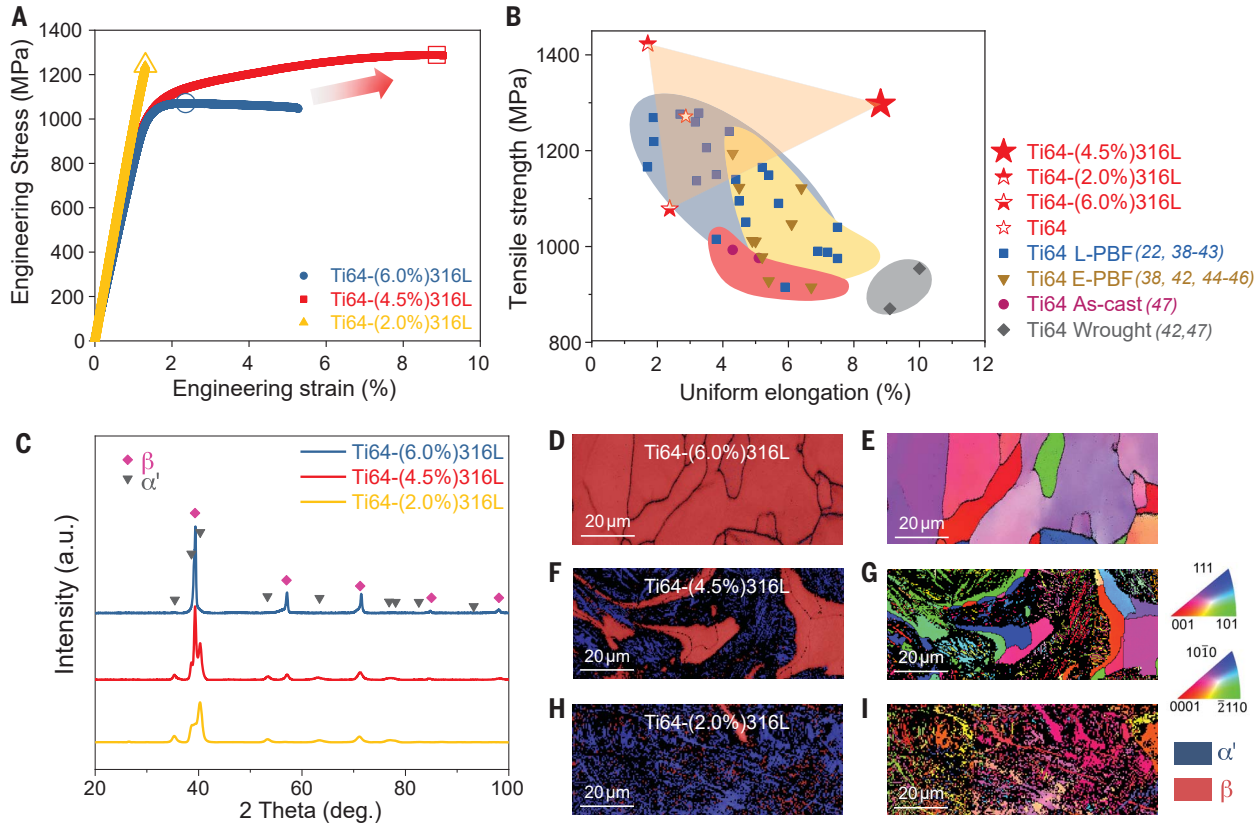

Fig. 2. Microstructure and mechanical properties of the as-printed microCM Ti64-x316L alloy. (**A**) Engineering stress-strain curves of as-printed Ti64-(6.0%)316L, Ti64-(4.5%)316L, and Ti64-(2.0%)316L alloys, respectively. The UTS is marked by big open symbols in the curves. (**B**) Engineering tensile strength versus uniform elongation of the as-printed Ti64-x316L alloy as compared with Ti64 alloy produced by different AM methods and conventional technologies (*22*, *38*–*47*). (**C** to **I**) Influence of microCMs on microstructure of Ti64-x316L alloys. (C) XRD profiles of phase constitution of three alloys. a.u., arbitrary units. [(D) to (I)] EBSD phase images and IPF maps of three different as-printed alloys showing phase constituents and grain orientations.

of mainly the β phase (Fig. 2, C to E) after printing but exhibits little work hardening during deformation (Fig. 2A). What is different about the retained β phase in Ti64-(4.5%)316L microCM alloy is that (i) it is largely metastable because of the amounts of Fe, Cr, Ni, and Mo elements present and (ii) it has a continuous variation in its metastability because of the continuous variations in Fe, Cr, Ni, and Mo concentrations (*28*). Those retained β phase regions with relatively high concentrations of these elements show higher mechanical stability under load and have higher triggering stresses for the stress-induced β-to-α′ martensitic transformation (SIMT) (*28*), whereas those β phase regions with relatively low concentrations of these elements have lower triggering stresses for SIMT (*28*). Thus, upon loading, the SIMT first starts within the less-stable β phase regions and then gradually propagates to those more-stable β phase regions as the applied load increases. This substantially enhances the work-hardening capacity of the microCM Ti64-(4.5%)316L alloy. The x-ray diffraction (XRD) patterns (Fig. 3A) show that, during deformation, the peak intensities of $(110)_\beta$ at 39.4° and $(200)_\beta$ at 57.5° decrease continuously. The calculated β phase fraction decreases from 58 to 25% after deformation, reflecting a continuous deformation-induced phase transformation from the metastable β phase to the α′ martensitic phase, which is also confirmed by the EBSD phase maps (Fig. 3, B and C). The stress-induced martensite is confined within the prior-β grains (Fig. 3D and fig. S8). By contrast, even though microCMs of the β stabilizers also exist in Ti64-(6.0%)316L, most of the β phase in this alloy is too stable (because of the high Fe, Cr, Ni, and Mo contents) to transform to the martensite during deformation (fig. S9), and thus, we did not observe a noticeable TRIP effect. A comparison of the incremental work-hardening behavior of the two alloys as a function of strain is shown in Fig. 3, E and F. After being strained at >2%, the Ti64-(6.0%)316L alloy exhibits a quick drop of the work-hardening rate to <600 MPa, with a small work-hardening exponent. On the contrary, the Ti64-(4.5%)316L alloy exhibits a much higher and gradually decreased work-hardening rate and a much higher and steady work-hardening exponent over a much larger strain range, which reflects a steady and continuous SIMT during the deformation (Fig. 3A).

The high strength of the as-printed microCM Ti64-(4.5%)316L alloy also originates from the fine and highly dispersed mixture of the α′ and metastable β dual-phase microstructure. As they accompany the modulated concentration, the super-refined α′ martensite regions or swirls are dispersed in between the β phase regions or swirls and show an average swirl spacing of ~5 μm between adjacent swirls, which provides a high yield strength to the alloy. When the amount of the 316L powders added is low, the as-printed Ti64-(2.0%)316L alloy comprises mainly super-refined α′ martensite (Fig. 2, C, H, and I) because of the low contents of the β stabilizers on average. The high fraction of the super-refined α′ martensite microstructure makes the alloy strong

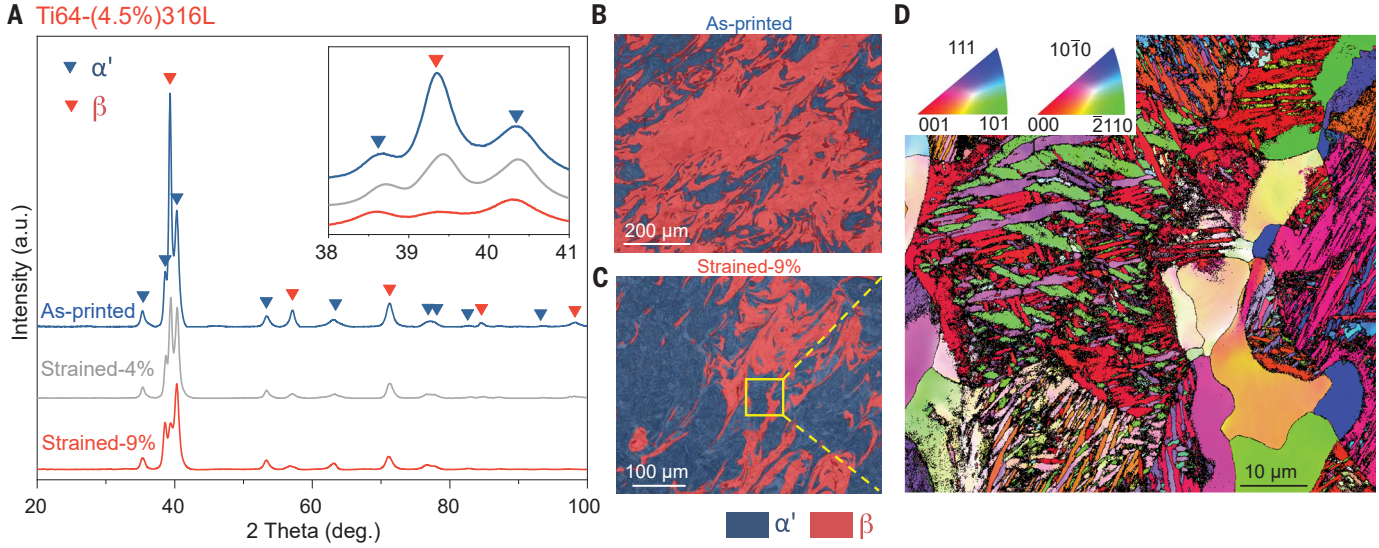

Fig. 3. Work-hardening behavior and microstructure evolution of the microCM alloys. (**A**) XRD profiles of the as-printed Ti64-(4.5%)316L alloy showing the continuous β → α′ phase transformation during tensile test. (**B** and **C**) EBSD phase images showing decrease of β phase volume fraction after being strained to failure. (**D**) Enlarged EBSD IPF map at the yellow box in (C) that shows the morphology of acicular α′ martensite and retained β grains after the tensile test. (**E**) Work-hardening rate curves of the microCM alloys. (**F**) Dynamic change of the work-hardening exponent versus true strain within the uniform deformation process of the microCM alloys.

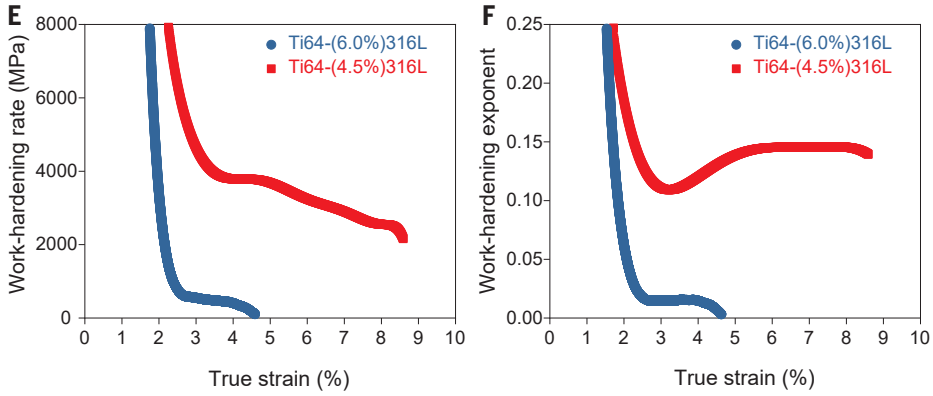

but brittle (Fig. 2A), having a yield strength of >1400 MPa but fracturing even before yielding for most samples. In view of this, the control of the mean of the microCM by controlling the amount of the 316L powders added is critically important for achieving the above-mentioned dual-phase microstructure for a balanced strength and ductility.

The third important impact of the microCM is on the grain refinement. As has been verified by the EBSD images (for example, Fig. 1H), we measured the average grain size of the as-printed Ti64-(4.5%)316L alloy as ~16 ± 6 μm, which is one of the finest grain structures achieved in an AM Ti alloy (Fig. 4A) (*35*–*37*). The grain size of the as-printed alloy is influenced to a large degree by its increased constitutional supercooling capacity, which is usually measured by the growth restriction factor Q-value (*25*). A high Q-value indicates a high constitutional supercooling, which activates more nuclei and restricts the growth of existing grains (*25*, *26*, *35*), which leads to a finer grain structure (*7*, *50*). On the basis of our Thermo-Calc calculations (Fig. 4B and fig. S10)

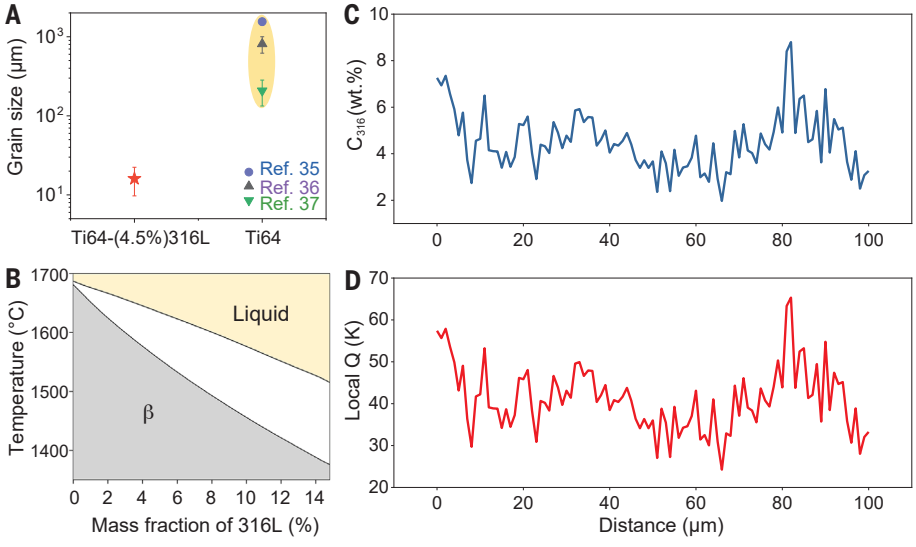

Fig. 4. Effects of microCM on grain refinement. (**A**) Comparison of average grain size between the as-printed Ti64 and microCM Ti64-(4.5%)316L alloys (*35*–*37*). (**B**) Pseudobinary Ti64-316L phase diagram calculated by Thermo-Calc software. (**C**) SEM-EDS long-time line scan curve shows the composition variation through several melt pools. (**D**) Calculated growth-restriction factor Q as a function of local composition on the basis of (C).

and combined with the measured local composition (Fig. 4C), the microCM Ti64-(4.5%)316L alloy is readily seen to have an average growth-restriction factor Q-value of ~40 K (Fig. 4D), which is about five times as much as that of Ti64 (Q ≈ 8 K). Because of the local variations of the 316L elements in the microCM alloy (Fig. 4C), a corresponding spatial variation of the Q-value (Fig. 4D) exists from ~24 K in the 316L element–poor regions to ~65 K in the 316L element–rich regions. The 316L element–rich β phase regions (higher Q-values) tend to have smaller grains as compared with those of the 316L element–poor α′ phase regions (smaller Q-values) (Fig. 1H).

We have demonstrated a method of microCM alloy design that is enabled by L-PBF with fine-scale concentration modulations for achieving adaptive microstructures with excellent mechanical properties. The microCM Ti64-(4.5%)316L alloy that is made through partial homogenization has a fine and highly dispersed mixture of α′ + metastable β dual-phase microstructure with fine grains (~16 μm) in its as-printed state. With the super-refined α′ phase regions offering the alloy a high yield strength and the continuous variations in Fe, Cr, Ni, and Mo concentrations in the retained metastable β phase regions offering the alloy a progressive TRIP effect in a broad stress range, the microCM Ti64-(4.5%)316L alloy exhibits a high tensile strength of ~1.3 GPa, a uniform elongation of ~9%, and an excellent work-hardening capacity of >300 MPa in its as-printed state. These excellent properties may enable many advanced applications of the microCM Ti alloys in the aerospace, automotive, chemical, and medical industries. We expect the microCMs to produce different types of spatially modulated phase stabilities and microstructures in different alloy systems (*16*, *17*, *19*, *20*), which will offer some distinctive properties that are superior to those of their homogeneous counterparts.

REFERENCES AND NOTES

1. D. Herzog, V. Seyda, E. Wycisk, C. Emmelmann, *Acta Mater.* **117**, 371–392 (2016).
2. W. E. Frazier, *J. Mater. Eng. Perform.* **23**, 1917–1928 (2014).
3. W. J. Sames, F. A. List, S. Pannala, R. R. Dehoff, S. S. Babu, *Int. Mater. Rev.* **61**, 315–360 (2016).
4. C. Panwisawas, Y. T. Tang, R. C. Reed, *Nat. Commun.* **11**, 2327 (2020).
5. Y. M. Wang *et al.*, *Nat. Mater.* **17**, 63–71 (2018).
6. J. H. Martin *et al.*, *Nature* **549**, 365–369 (2017).
7. D. Zhang *et al.*, *Nature* **576**, 91–95 (2019).
8. P. Kürnsteiner *et al.*, *Nature* **582**, 515–519 (2020).
9. S. A. M. Tofail *et al.*, *Mater. Today* **21**, 22–37 (2018).
10. T. M. Pollock, *Nat. Mater.* **15**, 809–815 (2016).
11. M. Zhang *et al.*, *Sci. Adv.* **6**, eaba5581 (2020).
12. D. Raabe, C. C. Tasan, E. A. Olivetti, *Nature* **575**, 64–74 (2019).
13. B. Vrancken, L. Thijs, J.-P. Kruth, J. van Humbeeck, *Acta Mater.* **68**, 150–158 (2014).
14. I. Yadroitsev, P. Krakhmalev, I. Yadroitsava, *JOM* **69**, 2725–2730 (2017).
15. D. Gu *et al.*, *Science* **372**, eabg1487 (2021).
16. T. Zhang, D. Wang, Y. Wang, *Acta Mater.* **196**, 409–417 (2020).
17. R. Ding *et al.*, *Sci. Adv.* **6**, eaay1430 (2020).
18. W. W. Sun, Y. X. Wu, S. C. Yang, C. R. Hutchinson, *Scr. Mater.* **146**, 60–63 (2018).
19. J. Zhu, D. Wang, Y. Gao, T.-Y. Zhang, Y. Wang, *Mater. Today* **33**, 17–23 (2020).
20. J. Zhu, Y. Gao, D. Wang, T.-Y. Zhang, Y. Wang, *Acta Mater.* **130**, 196–207 (2017).
21. B. E. Carroll, T. A. Palmer, A. M. Beese, *Acta Mater.* **87**, 309–320 (2015).
22. C. J. Todaro *et al.*, *Nat. Commun.* **11**, 142 (2020).
23. X. Wu *et al.*, *Mater. Des.* **25**, 137–144 (2004).
24. L. Thijs, F. Verhaeghe, T. Craeghs, J. van Humbeeck, J.-P. Kruth, *Acta Mater.* **58**, 3303–3312 (2010).
25. M. J. Bermingham, S. D. McDonald, M. S. Dargusch, D. H. StJohn, *J. Mater. Res.* **23**, 97–104 (2008).
26. D. Zhang *et al.*, *Metall. Mater. Trans., A Phys. Metall. Mater. Sci.* **51**, 4341–4359 (2020).
27. Materials and methods are available as supplementary materials.
28. C. Li, J. H. Chen, X. Wu, W. Wang, S. van der Zwaag, *J. Mater. Sci.* **47**, 4093–4100 (2012).
29. S. J. Clark *et al.*, *IOP Conf. Ser.: Mater. Sci. Eng.* **861**, 12010 (2020).
30. Q. Guo *et al.*, *Addit. Manuf.* **31**, 100939 (2020).
31. R. Cunningham *et al.*, *Science* **363**, 849–852 (2019).
32. W. Huang, H. Wang, T. Rinker, W. Tan, *Mater. Des.* **195**, 109056 (2020).
33. A. M. Vilardell *et al.*, *Addit. Manuf.* **36**, 101436 (2020).
34. M. Simonelli *et al.*, *Metall. Mater. Trans., A Phys. Metall. Mater. Sci.* **51**, 2444–2459 (2020).
35. M. J. Bermingham, D. H. StJohn, J. Krynen, S. Tedman-Jones, M. S. Dargusch, *Acta Mater.* **168**, 261–274 (2019).
36. Y. M. Ren *et al.*, *Acta Mater.* **132**, 82–95 (2017).
37. P. W. Liu *et al.*, *J. Mater. Process. Technol.* **257**, 191–202 (2018).
38. H. K. Rafi, N. V. Karthik, H. Gong, T. L. Starr, B. E. Stucker, *J. Mater. Eng. Perform.* **22**, 3872–3883 (2013).
39. T. Vilaro, C. Colin, J. D. Bartout, *Metall. Mater. Trans., A Phys. Metall. Mater. Sci.* **42**, 3190–3199 (2011).
40. W. Xu *et al.*, *Acta Mater.* **85**, 74–84 (2015).
41. G. Kasperovich, J. Hausmann, *J. Mater. Process. Technol.* **220**, 202–214 (2015).
42. L. Facchini *et al.*, *Rapid Prototyping J.* **16**, 450–459 (2010).
43. W. Xu, E. W. Lui, A. Pateras, M. Qian, M. Brandt, *Acta Mater.* **125**, 390–400 (2017).
44. C. de Formanoir *et al.*, *Acta Mater.* **162**, 149–162 (2019).
45. C. de Formanoir, S. Michotte, O. Rigo, L. Germain, S. Godet, *Mater. Sci. Eng. A* **652**, 105–119 (2016).
46. H. Gong *et al.*, *Mater. Des.* **86**, 545–554 (2015).
47. M. Niinomi, *Mater. Sci. Eng. A* **243**, 231–236 (1998).
48. T. Yang *et al.*, *Science* **362**, 933–937 (2018).
49. T. Voisin *et al.*, *Mater. Des.* **158**, 113–126 (2018).
50. M. A. Easton, D. H. StJohn, *Acta Mater.* **49**, 1867–1878 (2001).

ACKNOWLEDGMENTS

Funding: The authors from City University of Hong Kong (CityU) are grateful for the internal funding from City University of Hong Kong under the programs 9042635, 9360161, and 9380060. T.Y. and C.-T.L. are also grateful for the financial support from the Hong Kong Institute for Advanced Study (grant no. 9360157). D.W. and T.Z. acknowledge the support of the National Key Research and Development Program of China (grant no. 2016YFB0701302) and the National Natural Science Foundation of China (grants nos. 51671156 and 51671158). Z.H. acknowledges the GDAS's Project of Science and Technology Development (2019GDASYL-0203002). Y.W. acknowledges the support by the US National Science Foundation (grant DMR – 1923929). **Author contributions:** C.-T.L., Y.W., and T.Z. conceived the idea and designed the research. T.Z. designed the processing parameters and prepared the specimens. T.Z. characterized the specimens by means of SEM, EDS, EBSD, and XRD and conducted Thermo-Calc calculations. T.Z. and Z.H. performed the micro-CT analysis. Z.H. and A.W. operated the 3D printer and manufactured the samples. T.Y. carried out the TEM. J.L. conducted the 3D-APT. H.K. and T.Z. performed the mechanical testing. T.Z., C.-T.L., Y.W., T.Y., and D.W. analyzed the data and discussed the results. T.Z., Y.W., C.-T.L., T.Y., and W.K. wrote and revised the manuscript. All authors reviewed and contributed to the final manuscript. **Competing interests:** C.-T.L. and T.Z. are inventors on a US patent (application no. 17/012,507) that has been filed related to the alloy design described in this work. The rest of the authors declare no conflict of interests. **Data and materials availability:** All data are available in the main text or the supplementary materials.

SUPPLEMENTARY MATERIALS

science.org/doi/10.1126/science.abj3770
Materials and Methods
Figs. S1 to S11
Tables S1 and S2
References (*51*–*98*)

9 May 2021; accepted 8 September 2021
10.1126/science.abj3770

In situ design of advanced titanium alloy with concentration modulations by additive manufacturing

Tianlong ZhangZhenghua HuangTao YangHaojie KongJunhua LuanAnding WangDong WangWay KuoYunzhi WangChain-Tsuan Liu

Science, 374 (6566),

Fine-scale strengthening swirls

Creatively combining different alloys using additive manufacturing methods has the potential to produce materials with interesting properties. Zhang *et al*. use laser powder bed fusion to combine small amounts of 316L stainless steel into Ti64 titanium alloy. This process creates an alloy with a distinctive microstructure that retains high strength while substantially improving ductility. The design strategy should be useful for improving mechanical properties in other alloy system as well. —BG

Science (ISSN) is published by the American Association for the Advancement of Science. 1200 New York Avenue NW, Washington, DC 20005. The title *Science* is a registered trademark of AAAS.